Air–water properties of unsteady breaking bores part 1

Novel Eulerian and Lagrangian velocity measurements using intrusive and non-intrusive techniques

Shi, Rui; Wüthrich, Davide; Chanson, Hubert

Citation (APA)
Shi, R., Wüthrich, D., & Chanson, H. (2023). Air–water properties of unsteady breaking bores part 1: Novel Eulerian and Lagrangian velocity measurements using intrusive and non-intrusive techniques. *International Journal of Multiphase Flow*, *159*, Article 104338. https://doi.org/10.1016/j.ijmultiphaseflow.2022.104338

Important note
To cite this publication, please use the final published version (if applicable).
Please check the document version above.

Air–water properties of unsteady breaking bores part 1: Novel Eulerian and Lagrangian velocity measurements using intrusive and non-intrusive techniques

Rui Shi [a],[*], Davide Wüthrich [a],[b], Hubert Chanson [a]

[a] *School of Civil Engineering, The University of Queensland, St Lucia, Brisbane, 4067, QLD, Australia*
[b] *Department of Hydraulic Engineering, Delft University of Technology, Mekelweg 5, Delft, 2600GA, The Netherlands*

ARTICLE INFO

ABSTRACT

Transient motion, turbulence and bubble dynamics make any velocity quantification extremely difficult in unsteady gas–liquid flows. In the present study, novel Eulerian and Lagrangian techniques of velocimetry were developed, using both intrusive and non-intrusive measurements. The selected unsteady gas–liquid flow was a breaking bore, featured with a transient motion, air entrainment and coherent structures. Intrusively, Eulerian probe measurements resulted to the development of a single bubble event detection (SBED) technique in unsteady air–water flows. Non-intrusively, the motion of air–water pattern was detected using a novel particle tracking velocimetry (PTV). Both velocities obtained using SBED and PTV techniques were validated against the established optical flow (OF) results, achieving consistent velocity data among the three techniques. The filtering criteria of the SBED and PTV techniques were discussed, showing the best options in the breaking bore. It is concluded that the most robust velocity measurements in gas–liquid flow are achieved with consistent velocity data between the SBED, PTV and OF techniques.

1. Introduction

1.1. Experimental methods in gas–liquid flow

Unsteady gas–liquid flows are commonly found in nature (e.g. breaking waves, Tsunami and breaking bore) and in many engineering applications (e.g. bubble column flow, chemical reactor and pipe flow). When it comes to experimental investigations of these unsteady gas–liquid flows, the presence of gas bubbles affects adversely traditional velocity measurement techniques, such as particle image velocimetry (PIV), acoustic Doppler velocimetry (ADV) and Laser Doppler velocimetry (LDV), among others (Jones Jr. and Delhaye, 1976; Bachalo, 1994; Crowe et al., 1998). In particular, the bubbles randomly reflect signal for ADV and LDV, cause wrong pressure gradients in Pitot tube, and distort the laser beam for PIV.

The velocimetry in gas–liquid flow is classified into intrusive and non-intrusive techniques. Recent advances in image processing has led to a rapid growth on the application of the non-intrusive image based techniques. Ryu et al. (2005, 2007) modified a PIV cross-correlation technique to estimate the bubble velocity, introducing the bubble image velocimetry (BIV) in various air–water surface breakers. Alternatively, optical flow (OF) has recently attracted a lot attention in the air–water flow community (Bung and Valero, 2016; Zhang and Chanson,

2018). The OF is a well-developed branch from Computer Vision, detecting apparent motion between two consecutive video images. The difference between OF and BIV techniques is that OF detects the change in air–water flow patterns, thus calculating air–water interfacial velocity, while the BIV gives the bubble velocity distributions using cross-correlation in an interrogation window. A major challenge for the applicability of any optical technique (e.g. PIV, BIV, OF, PTV), based upon photographs and movies recorded through the sidewalls, is a substantial reduction in void fraction, bubble count rate and interfacial velocity compared to centreline air–water flow data (Bung and Valero, 2015; Zhang and Chanson, 2018).

The most reliable velocimetries are volumetric techniques (e.g. Gamma ray Hanus, 2015, tomography Warsito and Fan, 2001) and phase-detection needle probes (Cartellier and Achard, 1991). The first one is rarely used for large-scale flows, whereas the third one is more commonly used, including the optical fibre probe and conductivity/resistivity probe. The needle sensor size may typically be less than 0.1 mm in low velocity flows, while high velocity flow measurements require sturdier probe sensors, with sizes typically between 0.1 and 1 mm. A few studies used single-tip needle probes and obtained the

individual bubble velocity. One approach derives the bubble velocity based upon the slope if the probe signal during piercing (Sene, 1984; Cartellier, 1992; Cummings, 1996). Another method is based on the coherent beat signal between the Fresnel reflection off the fibre–liquid interface and the scattered signal off the bubble (Chang et al., 2003). Older bubble detection techniques, sometimes called individual droplet/bubble impact detection, gas–liquid pattern recognition or multi-channel techniques, have been used with dual-tip phase-detection probes for several decades in gas–liquid flows (Serizawa et al., 1975; Kocamustafaogullari and Wang, 1991; Liu and Bankoff, 1993). While most applications were in steady gas–liquid flows in pipes, Wang and Chanson (2019) and Chanson (2005) undertook individual bubble velocity in highly fluctuating free-surface flows and a dam-break wave respectively.

To date, limited velocity measurements have been conducted in unsteady self-aerated flows, such as breaking waves and breaking bores, with a few exceptions. The phase-averaging flow characteristics were derived using image-based methods and synchronisation in breaking waves (Kimmoun and Branger, 2007; Na et al., 2020). Shi et al. (2020) considered the breaking bore quasi-steady, combining synchronisation and optical flow to obtain dense velocity contours in the breaking bore roller. Their subsequent work (Shi et al., 2021) further quantified two-dimensional turbulence in the breaking bore roller.

1.2. Unsteady gas–liquid flow: a breaking bore

A breaking bore can form during many natural processes, including tidal bores induced by moon gravity in river estuary (Chanson, 2012) (Fig. 1), tsunamis reaching the shoreline, breaking waves when the wave face is fully turbulent (Peregrine, 1983) and dam-break waves propagating on wet bed (Stansby et al., 1998). Based on quasi-steady flow analogy, a breaking bore can be considered as a hydraulic jump in translation (Lighthill, 1978). The strength of the bore is characterised by its bore Froude number:

$$Fr_1 = \frac{V_1 + U}{\sqrt{gA/B}} \tag{1}$$

where g is the gravitational constant, V_1 is the cross-sectional averaged velocity of initial flow, U is the mean bore celerity, A is the channel area and B is the free-surface width. A fully breaking bore, observed for $Fr_1 > 1.6$ (Leng and Chanson, 2016), exhibits large-scale coherent structures, air entrainment and strong free surface turbulence (Fig. 1). The bore propagation is seen as an increase in water level. This sudden change of the flow streamline triggers several flow instabilities (Lubin et al., 2019), where the significant shearing causes the large-scale vortices, observed as the white "roller". The white colour represents the air–water mixture, where the air is entrained into the bore by extrusion and free-surface motion (Kiger and Duncan, 2012). The rolling vortices contribute to the strong free surface turbulence (Brocchini and Peregrine, 2001; Wüthrich et al., 2021), and to the entrapment and convection of the air bubbles in the breaking roller (Leng and Chanson, 2019). The intense bubble-turbulence interactions result into random bubble shapes and a large region of air–water mixture in the breaking roller, which enhanced the difficulty for velocity measurements in the breaking roller.

In the present study, the breaking bore was selected as the targeted unsteady gas–liquid flow, focusing on the velocity measurements in part 1 and air–water characteristics in part 2. The comprehensive datasets were achieved using several novel experimental techniques, which were also developed for the applications to general gas–liquid flows. For this paper, the Eulerian velocimetry was achieved by a novel signal processing technique using a intrusive phase-detection probe array, deriving pseudo-instantaneous velocity. The Lagrangian approach is referred to a particle tracking velocimetry (PTV) technique, obtaining the two-dimensional trajectories in the aerated flow region. Both novel techniques were validated against a well-established optical flow approach.

2. Experimental facility and instrumentation

2.1. Experimental setup

A new series of experiments was performed in a large-size facility at the University of Queensland, Australia. It consisted of a 19 m long, 0.7 m wide, and 0.5 m high rectangular channel and water supply system. The channel was made with a smooth PVC invert and glass sidewalls. The water was introduced to the channel through an upstream water tank, where flow straighteners were installed to calm the initial flow. The flow discharge was measured through a magneto flow metre with an accuracy of 10^{-5} m^3/s. The maximum discharge of 0.10 m^3/s was achieved using two pumps. A Tainter gate was located at the downstream end of the channel (Fig. 2). By rapidly closing the gate, a sudden increase in water depth induced a positive surge or bore propagating upstream (Fig. 1c). The closure time was less than 0.2 s, minimising the impact of the generation process on the bore characteristics. The breaking bore generated using the gate closure was highly repeatable, thus leading to a high number of experimental runs for ensemble statistics.

2.2. Instrumentation

The air–water flow signals were simultaneously recorded using an array of three dual-tip phase-detection probes (Fig. 2), equipped with two needle sensors with an inner silver electrode (0.25 mm diameter) and outer stainless-steel electrode (0.80 mm diameter). Fluoropolymer of tetrafluoroethylene (PTFE) insulation was placed between the inner and outer electrodes, forming a closed circuit when the probes were in contact with water. The two needle sensors had different length with a longitudinal separation distance $\Delta x = 0$ m, 0.0051 m and 0.0071 m for the three probes. The probe with $\Delta x = 0.0051$ m was placed on the channel centreline, measuring the flow characteristics that were the least affected by the channel sidewall. The probe of $\Delta x = 0$ m was 0.05 m beside the centre probe, and was located at 0.005 m above the initial flow surface. This is so-called reference probe, and was used as the time reference for the bore arrival (Chanson, 2005). The last probe ($\Delta x = 0.0071$ m) provided the sidewall measurements, denoted as sidewall probe. The sidewall probe was 4–5 mm from the sidewall, which was the closest location due to the technical limitations. Both centreline and sidewall probes were simultaneously moved in the vertical direction. The leading tip sensors of the three phase-detection probes were located at $x = 8.5$ m, and were sampled at 100 kHz. The vertical position of the probe sensors was measured using a magnetic reader with a precision of $\pm$0.1 mm. Detailed probe set-up is shown in Fig. 3c.

The flow motions were recorded using a Phantom v2011 ultra-high-speed video camera, equipped with a lens Zeiss^{TM} Planar T$*$85 mm f1.4D (Fig. 3). The camera was capable of recording 22,604 frames per second (fps) with a full HD (1280 × 800) resolution. The camera was installed on the side (Fig. 3a), with a visualisation window of 0.52 m long and 0.38 m wide. The camera focused on the flow about 3–4 mm from the sidewall, and the depth of field was approximately 15 mm. The camera was sampled at 10,000 fps in full HD resolution, with an intensive Light Emitting Diode (LED) array to maximise the lighting and illumination of the flow features. The phase-detection probes recorded the air–water flow signals at 20 vertical locations in the range of $0.82 \leqslant z/d_1 \leqslant 2.85$, with 100 repetitions for each location, z being the vertical elevation and d_1 the initial flow depth. For 20 repetitions at 16 vertical locations, the three phase-detection probes and the ultra-high-speed camera were sampled simultaneously. The synchronisation tests between probes and camera showed a median time lag of 1.4×10^{-4} s.
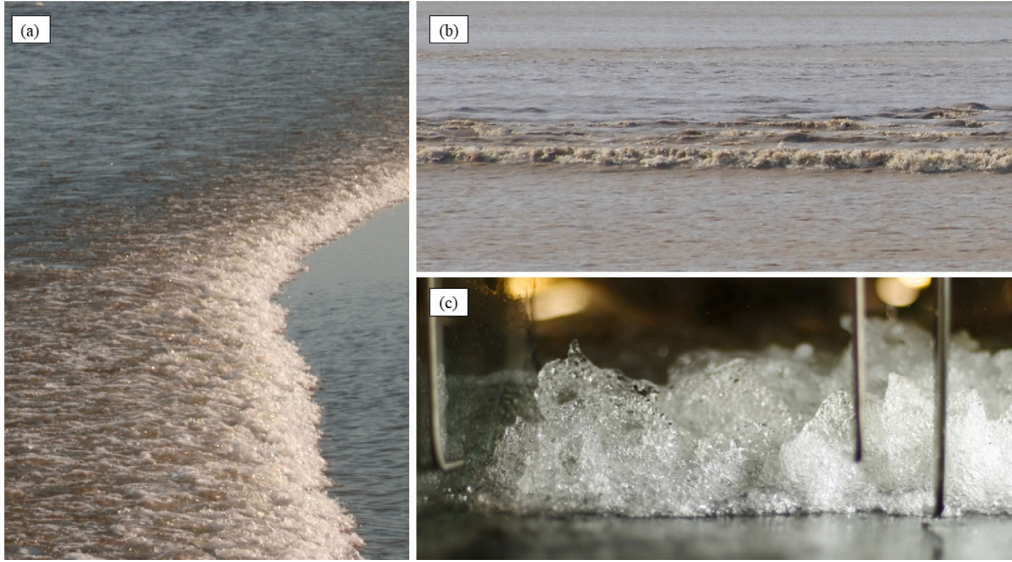
Fig. 1. Breaking bores — (a) Breaking tidal bore of the Sélune River near Avranches (France) on 18 April 2018 with roller propagation from left to right (Photograph by H. Chanson); (b) Breaking tidal bore of the Garonne River upstream of Bordeaux (France) on 5 July 2019, with roller propagation from background to foreground (Photograph H. Chanson); (c) Breaking bore roller propagation at the University of Queensland, with roller propagation from background to foreground (Fr_1 = 2.4, shutter speed: 1/2,000 s) (Photograph H. Chanson) — Note the array of three dual-tip phase-detection probe, with the sensors facing the incoming roller.
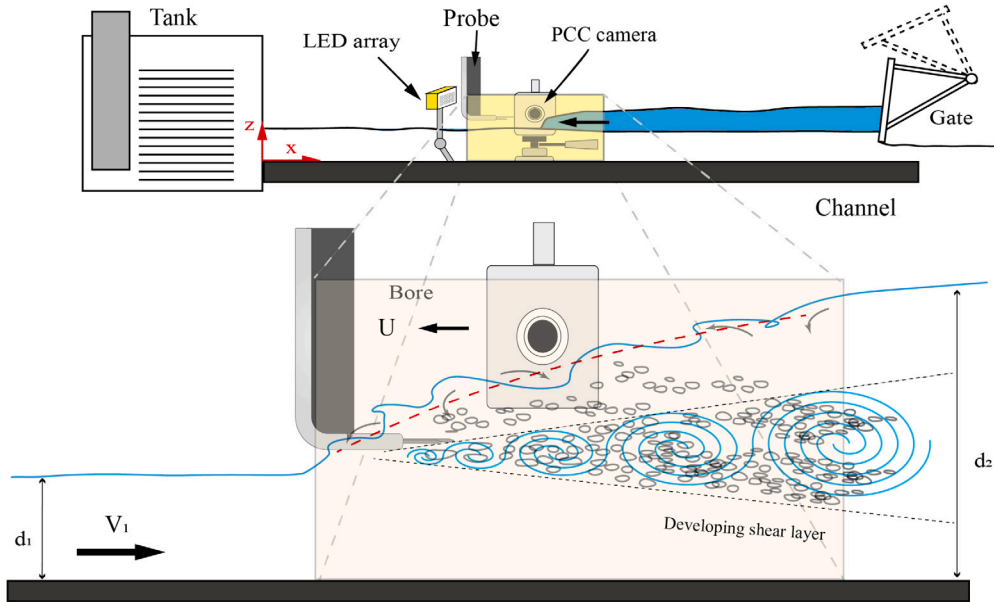

Fig. 2. Sketch of the experimental set-up and instrumentation. The initial flow is issued from left to right, with the bore propagating in opposite direction.

2.3. Flow conditions

The present study adopted the positive x coordinate being consistent with the initial flow direction, positive z coordinate pointing upwards with zero at the channel bed, and positive y coordinate point being perpendicular to the side walls with zero from the channel size away from the camera. The mean bore front celerity (U) was measured using the bore travel distance over travel time. The travel time and water depth were derived from three acoustic displacement metres (ADMs) placed at x = 7.0, 8.5 and 10.0 m on the channel centreline. The initial flow depth was d_1 = 0.084 m, and the bore conjugate depth was d_2 = 0.245 m. The flow rate was Q = 0.1 m³/s, giving an initial flow velocity of V_1 = 1.707 m/s based on continuity equation. These flow conditions gave the Reynolds number Re = 2.03 × 10⁵, defined as $Re = d_1(V_1 + U)/\upsilon$, with υ the kinematic water viscosity. The bore Froude number was Fr_1 = 2.4.

3. Single bubble event detection (SBED) technique

3.1. Presentation

The phase-detection probe was first introduced in gas–liquid flow by Neal and Bankoff (1963). The principle of the phase-detection needle probe is the distinctive response between air and water. Through successive interface piercings, the probe signal presents square-wave-like response. The raw signal is typically binarised using a single-threshold technique (Cartellier and Achard, 1991), yielding the instantaneous void fraction signal $c(t)$, in which zero and one indicate gas and liquid phases respectively. For steady gas–liquid flow, the time-averaged void fraction and bubble chord time can be derived from $c(t)$ (Chanson and Toombes, 2002), while the interfacial velocity measurements are based upon the differences in signal outputs between the leading and trailing
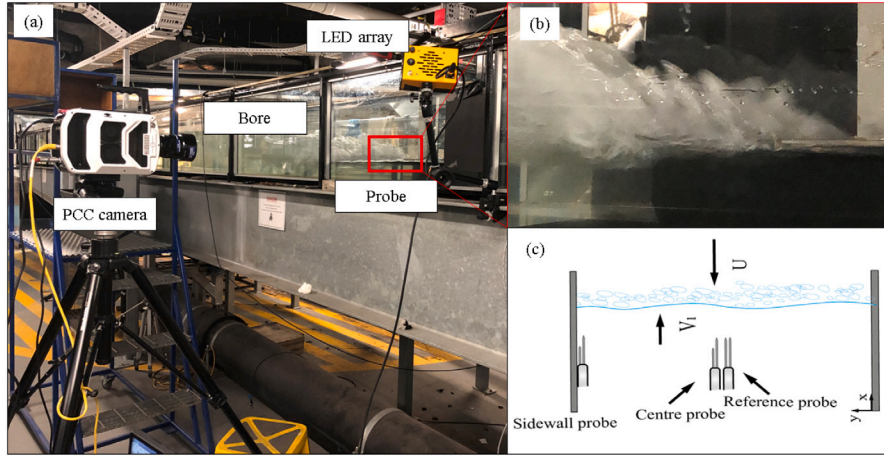
Fig. 3. Illustrations of experimental set-up and instrumentation (a) experimental set-up; (b) a side-view photo with the bore propagation from right left; (c) sketches of the top-view.

sensors of a dual-tip phase-detection probe. A cross-correlation between leading and trailing tip signals provides the characteristic convection time (τ) of interfaces between the two sensors, thus the interfacial velocity $\overline{V_x} = \Delta x / \tau$. This approach, denoted as traditional cross correlation (TCC) technique, has been widely adopted in air–water flows with high void fractions (Jones Jr. and Delhaye, 1976; Crowe et al., 1998; Chanson and Toombes, 2002). Some intrinsic limitations of the TCC technique include a need for steady flow conditions, an output that is a spatial average across the two sensors, suspiciously high turbulence intensity data, the inability to measure fluctuating velocities about zero with infinite convection time for zero velocity, the adverse impact of the leading tip on the trailing tip.

Based on the TCC technique, Kramer et al. (2019) introduced the adaptive window cross-correlation (AWCC) technique, which divided the signals into small window with a certain number of air–water particles. The instantaneous velocity was extracted from each window, with the application of several filtering technique. This modification significantly improved the turbulence intensity data, and various validation tests were performed in the following work (Kramer et al., 2020). So far, the AWCC technique is capable of providing high quality data in the steady air–water flows, thus motivating the present single bubble event detection (SBED) technique for targeting unsteady air–water flow. Herein, the SBED technique adopted the concept of small window cross-correlation approach from the AWCC technique (Kramer et al., 2020), and was added steps and filters to cope the unsteadiness of the flow in the signal processing.

3.2. Signal processing

The SBED technique was directly related to the work of Kramer et al. (2020), which means that some similarities can be observed for the following equations from the AWCC technique. The signal processing started with the single-threshold criteria (Cartellier and Achard, 1991), which was used to translate both leading S_L and trailing S_T tip signals into instantaneous void fraction signal $c(t)$, based on the 50% of the difference between averaged air $\overline{Vo_a}$ and water $\overline{Vo_w}$ voltages:

$$\frac{S_{L \, or \, T} - \overline{Vo_a}}{\overline{Vo_w} - \overline{Vo_a}} \begin{cases} \geq 0.5 \Rightarrow c(t) = 1 & \text{air} \\ < 0.5 \Rightarrow c(t) = 0 & \text{water} \end{cases} \tag{2}$$

An example of instantaneous void fraction $c(t)$ for the probe tip is presented in Fig. 4. Using the reference probe signal, the bore arrival time t_0 was defined as the time instant when the reference probe detected the first air–water interface. For the sidewall and centreline probes, the first air–water interface occurred at t_1, thus giving a relative time $t_r = t_0 - t_1$, where t_r could be negative value due to the non-uniform distribution of the roller toe in the transverse direction. Subsequently,

the air and water chords were identified from the $c(t)$ signal, enabling the signal segmentation. Two cases were then considered in this study: case 1: the phase-detection probe was placed beneath the initial water depth, and the first phase was water phase ($z/d_1 < 1$), case 2: the phase-detection probe was placed above the initial water depth ($z/d_1 > 1$), and the first phase was air phase. For the nth air chord time of the trailing tip signal $(t_{ch})_{Ta,n}$, a start time of the air phase was computed as

Case 1 ($z/d_1 < 1$) $t_{a,n} = t_r + \sum (t_{ch})_{Ta,n-1} + \sum (t_{ch})_{Tw,n}$ (3)

Case 2 ($z/d_1 > 1$) $t_{a,n} = t_r + \sum (t_{ch})_{Ta,n-1} + \sum (t_{ch})_{Tw,n-1}$ (4)

where $(t_{ch})_{Tw,n}$ is the nth water chord time of the trailing tip signal. This characteristic time instant was used to initialise the segmentation of the air–water flow signals. Since the time instant was defined from the trailing tip, the bubble might be detected from the leading tip. Thus, a backward time step was considered, as if the leading tip had captured any bubbles in a short duration. Herein, this short duration was defined as the preceding water chord time of the air chord time $(t_{ch})_{Ta,n}$. The segment existed only if the leading tip detected a bubble within in the time frame defined as:

Case 1 $t \subseteq [t_{a,n} - (t_{ch})_{Tw,n-1}, \ t_{a,n}]$
                                                                                                          (5)
Case 2 $t \subseteq [t_{a,n} - (t_{ch})_{Tw,n}, \ t_{a,n}]$

If a bubble was defined in the segment of the leading tip signal, the air-chord time of this bubble $(t_{ch})_{La,n}$ was extracted, and was used to define the small window as

Starting time $t_{n,1} = t_{a,n} - (t_{ch})_{La,n}$
                                                                                                          (6)
Ending time $t_{n,2} = t_{n,1} + (t_{ch})_{Tw,n+1}$

Fig. 5 illustrates the detection of the small windows for both cases. Then, the cross-correlation between the leading tip signal $S_{L,n}$ and trailing tip signal $S_{T,n}$ was computed, in line with a number of previous studies, including (Kramer et al., 2020):

$$R_{LT,n}(\tau) = \frac{\sum_{t_{n,1}}^{t_{n,2}} [(S_{T,n}(t) - \overline{S_{T,n}(t)})(S_{L,n}(t+\tau) - \overline{S_{L,n}(t)})]}{\sqrt{(\sum_{t_{n,1}}^{t_{n,2}})(S_{T,n}(t) - \overline{S_{T,n}(t)})^2} \sqrt{(\sum_{t_{n,1}}^{t_{n,2}})(S_{L,n}(t+\tau) - \overline{S_{L,n}(t)})^2}} \tag{7}$$

where τ is the time lag of cross-correlation function. The time lag of the maximum cross-correlation coefficient $R_{LT,n,max}$ was a characteristic travel time of the single bubble from the leading to trailing tip. The pseudo-instantaneous longitudinal velocity at time $t_n = (t_{n,1} + t_{n,2})/2$ for the single bubble event was expressed as:

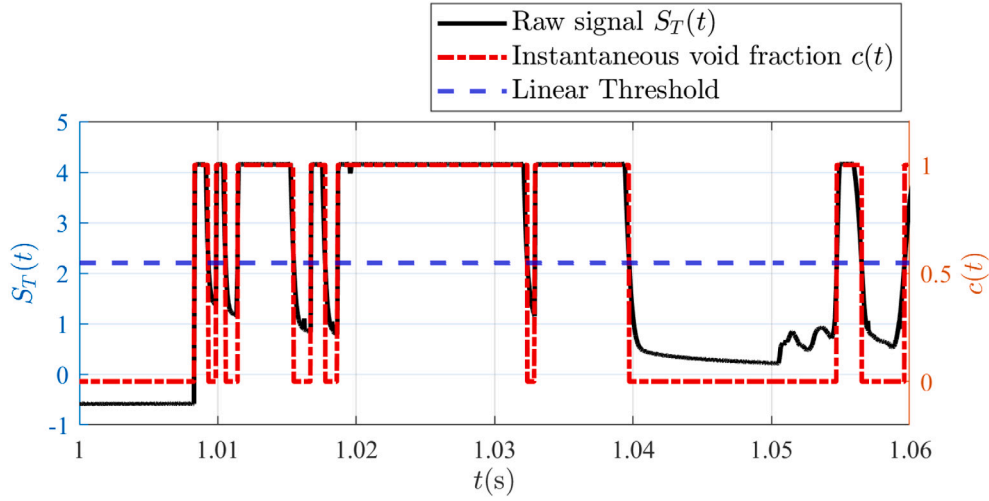$$v_{n,x} \approx [\overline{v}]_{t_{n,2}}^{t_{n,1}} = -\frac{\Delta x}{T_n} \tag{8}$$

Fig. 4. A typical example of instantaneous void fraction signal $c(t)$ using single threshold technique.
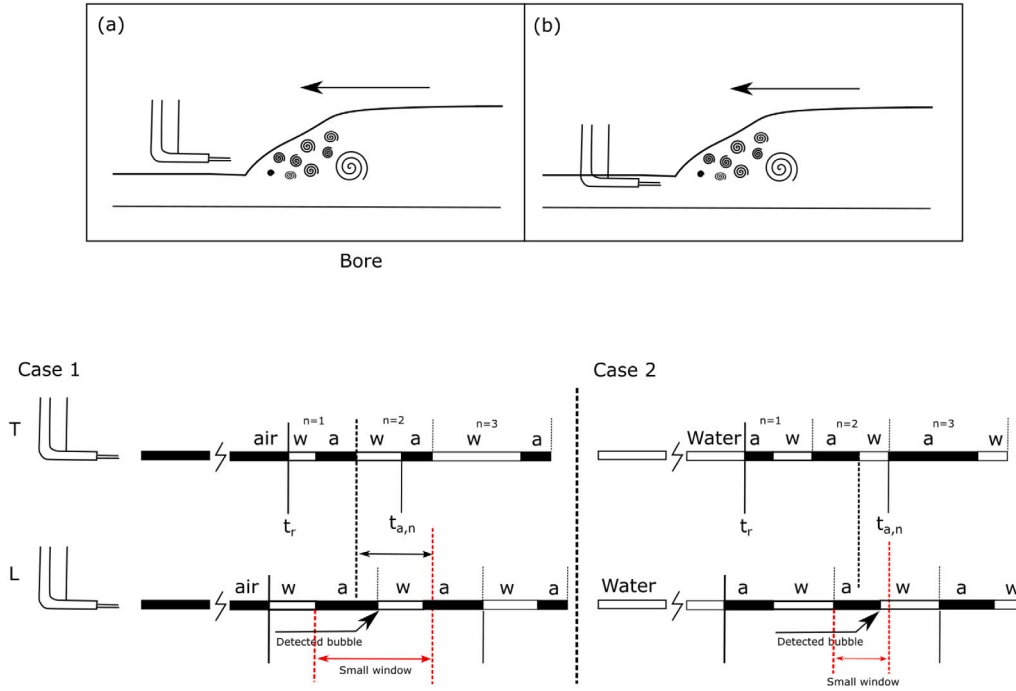

Fig. 5. Illustration of single bubble detection technique in air and water phases — (a) probes in air; (b) probes in water.

where T_n is the time lag between the leading and trailing tip signals of the small windows. Note that a negative sign was added in the above equation, aligning with the bore propagation direction.

One issue encountered during the study was the small number of bubbles detected by the probes during each experimental repetition. Herein, an experimental run (i.e. one repetition) corresponded to the probe signal data recorded from the bore generation until the bore reached the upstream end of the channel. In the shear layer, where the bubble concentration was the highest, the probe typically detected around 10–30 bubbles per run. With the filtering techniques introduced below, there were insufficient data during one run (i.e one repetition). Each experiment was therefore repeated multiple times, and the pseudo-instantaneous velocity data were combined. A sensitivity analysis on the number of repetitions is presented in Appendix A.1, showing that 50 tests were required to achieve robust and meaningful trends. In the present study, 100 repetitions were used at each vertical location for a comprehensive dataset.

The performance of the single bubble event highly relies on the cross-correlation of the small windows. Fig. 6 presents several examples of cross-correlation functions for selected the small time windows, as well as their results from the SBED technique. The small windows, sometimes, provided multiple cross-correlation peaks (Fig. 6 c), which might induce outliners. Alternatively, uncertainties were induced from transverse bubble impact, bubble breakup and coalescence. Namely, the leading and trailing tips detected different bubble events in a time window. This was reflected by the extreme value of T_n and low $R_{LT,n,max}$. Therefore, several filtering criteria were applied in SBED technique, involving the maximum cross-correlation coefficient $R_{LT,n,max}$, the ratio between absolute value of interfacial travel time and the window duration $|T_n|/W_n$ and secondary peak ratio (SPR), where SPR was defined as the ratio between the secondary cross-correlation peak and the maximum cross-correlation peak. A sensitivity analysis of the three criteria revealed that the optimal combination was given
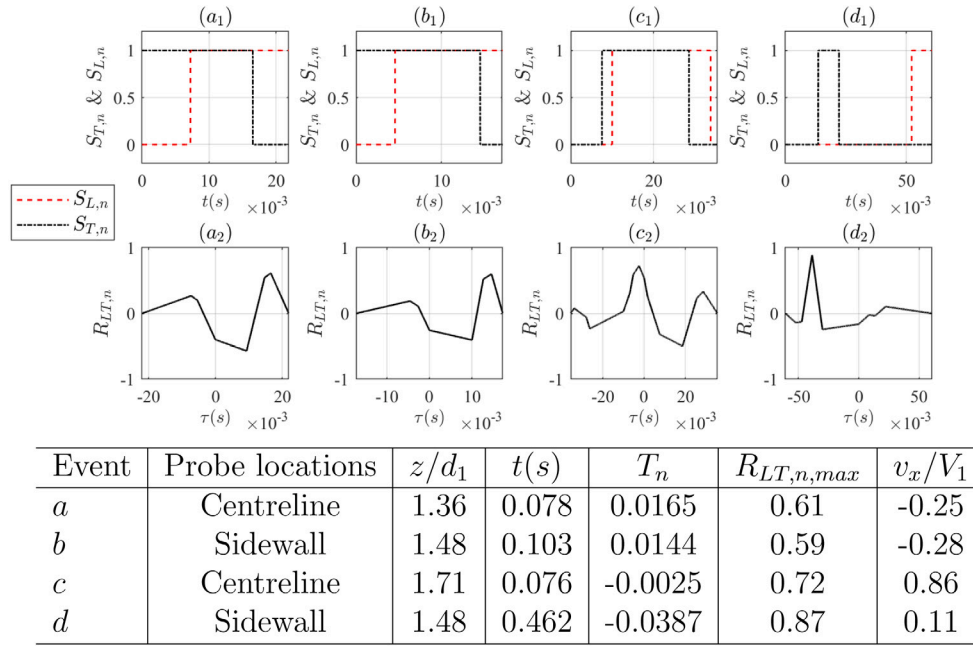
Event	Probe locations	z/d_1	$t(s)$	T_n	$R_{LT,n,max}$	v_x/V_1
a	Centreline	1.36	0.078	0.0165	0.61	-0.25
b	Sidewall	1.48	0.103	0.0144	0.59	-0.28
c	Centreline	1.71	0.076	-0.0025	0.72	0.86
d	Sidewall	1.48	0.462	-0.0387	0.87	0.11

Fig. 6. Leading and trailing tip signals of a time window (first row), as well as their cross-correlation function (second row).

by $R_{thres} = 0.4$ and $W_{thres} = 0.3$ and $SPR_{thres} = 0.5$. More details on sensitivity analysis are presented in Appendix A.2.

3.3. Validation

The validation dataset was derived from the ultra-high-speed videos using the OF technique. The OF technique is discussed in Appendix B. For the comparison with the phase-detection probe, a virtual probe function was added to the OF computation. This is, the time-series of the instantaneous OF velocity was extracted in a small image region, which had the same area of the probe tip sensor. Since several pixels were covered in this image region, the average OF velocity in this region were used. Note that the instantaneous OF velocity is always affected by the image noise, and the present OF data were filtered using the threshold technique of Kramer and Chanson (2019) and Kramer et al. (2020). The pseudo-instantaneous velocity data obtained with the SBED technique was based on the experimental data of 100 runs, thus the ensemble-averaged OF velocity were considered more comparable to the SBED data than the instantaneous OF velocity data.

Some comparisons between the time series of SBED and OF techniques are shown in Fig. 7, where the positive longitudinal velocity is downstream in line with the initial flow, and opposed to the bore propagation direction. The comparison showed a good agreement between the velocity data using the SBED and OF techniques, in terms of magnitude and trend (Fig. 7). Smoother velocity distributions were observed for OF data, because of the noise reduction associated with filtering and ensemble-averaging. The results of the SBED technique exhibited frequent changes in velocity sign for $t < 0.5$ s, corresponding to the vortical motions in the roller, but not captured in the ensemble-averaged OF data.

4. Particle tracking velocimetry (PTV)

4.1. Presentation

Particle tracking velocimetry (PTV) is a non-intrusive image-based technique, measuring trajectories and velocities of moving particles in the fluid. PTV is a Lagrangian approach, in contrast to the phase-detection probe which is typically Euleria, while the OF technique could be used as both Lagrangian and Eulerian approaches. In the

present study, the OF technique detected apparent motions in consecutive frames, thus implying that it was used with an Eulerian approach. There exist numerous works on PTV for laboratory fluid experiments, most of which tracked solid inertia particles (Oliveira et al., 2015; Fuchs et al., 2017; Ahmadi et al., 2019). For gas–liquid flow, the reflection of bubbles significantly impact the trajectories of solid particles, and low-density bubbles with regular shape (e.g. elliptical shape) were regarded as tracers (Nezu and Sanjou, 2011; Ziegenhein and Lucas, 2019). In the present study, the bubbles in the breaking roller exhibited highly non-regular shape under the strong turbulence. Thus, the PTV technique was more likely to detect the motion of air–water flow pattern, instead for individual bubbles. The aim of this PTV technique was to obtain the trajectories of the air–water cloud (contained bubbles with irregular shapes) in highly turbulent air–water flow. The computation was carried out using an open source software, Fiji ImageJ (Abràmoff et al., 2004).

4.2. Image processing

For the present study, it was impossible to analyse the large amount of bubbles with semi-automated or manual tracking, hence requiring automated tracking. The PTV was performed using the plugin TrackMate in Fiji ImageJ (Tinevez et al., 2017). TrackMate provides comprehensive tracking solutions, and is an extensible platform where researchers can further develop the algorithms to meet their needs. TrackMate included automated, semi-automated and manual tracking modules.

Fig. 8 presents an application of TrackMate to a local region of breaking bore roller, including 7 steps and 3 main output spreadsheets. The first step was the pre-processing, which removed the image noise by a median filter, while preserving clarity of the image in terms of focus. For the step 2, the background information was minimised by the "roller ball" algorithm, which is build-in function that removed unevenly illuminated background noise. Then, among the multiple options in ImageJ, a suitable algorithm was chosen to obtain the particles in the image plane. The present study used the LoG detector, which avoided the detection of small paper-salt noise and the bubble reflection.

The estimated particle diameter and thresholds were selected at step 4. The bubble-size distribution using image-processing showed that
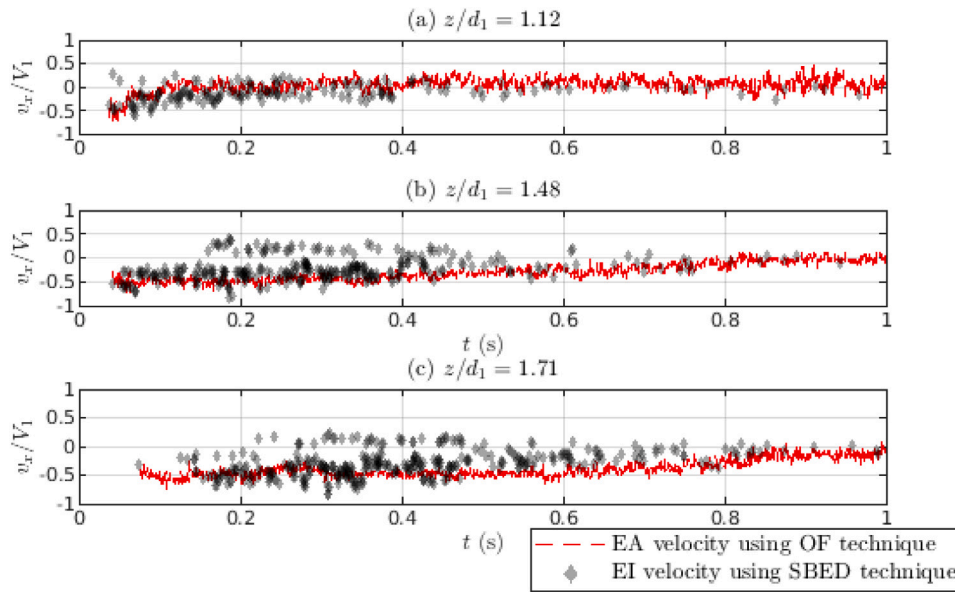
Fig. 7. Comparisons of time series between ensemble-instantaneous (EI) velocity data using SBED technique and ensemble-averaged (EA) velocity data using OF technique at different elevations in the breaking bore roller (a) lower region of the bore roller $z/d_1 = 1.12$ (b) middle region of the bore roller $z/d_1 = 1.48$ (c) upper region of the bore roller $z/d_1 = 1.71$.

most bubbles had a pseudo-diameter of 5–15 pixels, hence a diameter of 10 pixels was selected. The LoG detector highlighted all the particles, as shown for the step 4 in Fig. 8. The step 5 involved the selection of the tracker. TrackMate includes the Linear Assignment Problem (LAP) tracker (Jaqaman et al., 2008) and nearest neighbour search tracker. The former is capable of dealing with gap-closing events, and it is optimal since the bubble exhibited sudden brightness changes due to the surface reflection. The latter was used for three-dimensional tracking, which is not the objective of the present study. In addition, the advanced LAP option considered the splitting and merging event. The bubbles generated from breaking-down and coalescence were considered as different bubbles.

Using the LAP tracker, three parameters needed to be determined, including the linking maximum distance (LMD) D_L, gap-closing maximum distance (GMD) D_G, and gap-closing maximum frame gap (GMFG) F_G. The LMD (D_L) limits the spatial detection range for the matching particles. The GMD (D_G) is the maximum spatial detection range when gap-closing event occurs, with its unit in pixel. For example, if the particle disappeared in the nth frame, the same particle in the $(n-1)^{th}$ frame and $(n+1)^{th}$ frame shall not separate more than the gap-closing max distance. The GMFG F_G is the maximum number of frames that a particle can disappear. With these values, all the frames were computed using the LAP algorithm, obtaining all the particle trajectories. The final step was to further filter these trajectories by applying a threshold on the number of spots in track. The purpose of the filtering was to discard short trajectories, which were caused by the image noise and bubble–bubble interactions. The filtered trajectories are presented for the step 7 in Fig. 8.

4.3. Sensitivity analyses and validation

Several parameters were carefully selected for the PTV technique, including the frame rate, D_L, D_G, F_G and the thresholds of trajectory T_{thres}. A sensitivity analysis was performed for these parameters, using an ultra-high-speed video with duration of 0.06 s, corresponding to 600 frames. Note that the flow over the short duration of 0.06 s was assumed to be in a quasi-steady condition.

The particle detection of the PTV was sensible to the increasing image noise from higher frame rate. An ultra-high-speed video (10,000 fps) was subsampled down to 1000 fps, 2000 fps, 3000 fps and 5000

fps. Fig. 9 presents the trajectories of same particles for selected frame rates. The videos of 1000 and 2000 fps provided smoother particle trajectories, while the noisy trajectories at higher frame rates might be associated with the PTV algorithms detecting the motions of surrounding bubbles due to short displacement under high frame rate. Therefore, a frame rate of 1000 fps was used for the PTV technique.

In the breaking roller, the dense bubble distributions and non-regular bubble shape resulted into a difficult selection of D_L, D_G and F_G values. Herein, a sensitivity analysis was conducted for $D_L = 0, 5, 10$ and 15, $D_G = 0, 5, 10, 15$ and 20, $F_G = 1, 5, 10$ and 20 and $T_{thres} = 1, 5, 10$ and 20. All combinations of these parameters were tested, but only representative results are presented. Fig. 10a & b present all trajectories of two combinations, where the top and bottom rows are the longitudinal and vertical velocity data respectively. Overall, the data of two combinations exhibited similar trends, except for less dense data in the downstream side of the bore in 10a. For the comparison, the OF technique was applied to the short video, and the time-averaging over 0.06 s was assumed to give pseudo-instantaneous values. The OF results are presented in Fig. 10c, showing better agreements with the data in Fig. 10b. Thus, it was concluded that the PTV approach using TrackMate was capable to obtain reliable velocity data, and that the parameters required a detailed sensitivity analysis. In the present study, the parameters $D_L = 10$ pixels, $D_G = 10$ pixels, $F_G = 2$ frames and $T_{thres} = 5$ were adopted for all video processing.

5. Results

5.1. Eulerian velocity data using SBED and OF techniques

The intrusive probe measurements were performed at 20 vertical locations, covering the entire aerated region of the roller. At each elevation, the instantaneous velocity data were obtained from 100 repetitions, delivering sufficient velocity values to fully characterise the flow. Herein, the time origin $t = 0$ indicated the bore arrival time, defined as the mean arrival time between the 2 tips of the reference probe. At each location, the time series of the pseudo-instantaneous velocity was obtained from 100 tests. The left column in Fig. 11 presents the velocity magnitude distributions on the channel centreline and next to the sidewall. The velocity magnitude data were used for a better interpretation, since the pseudo-instantaneous velocity
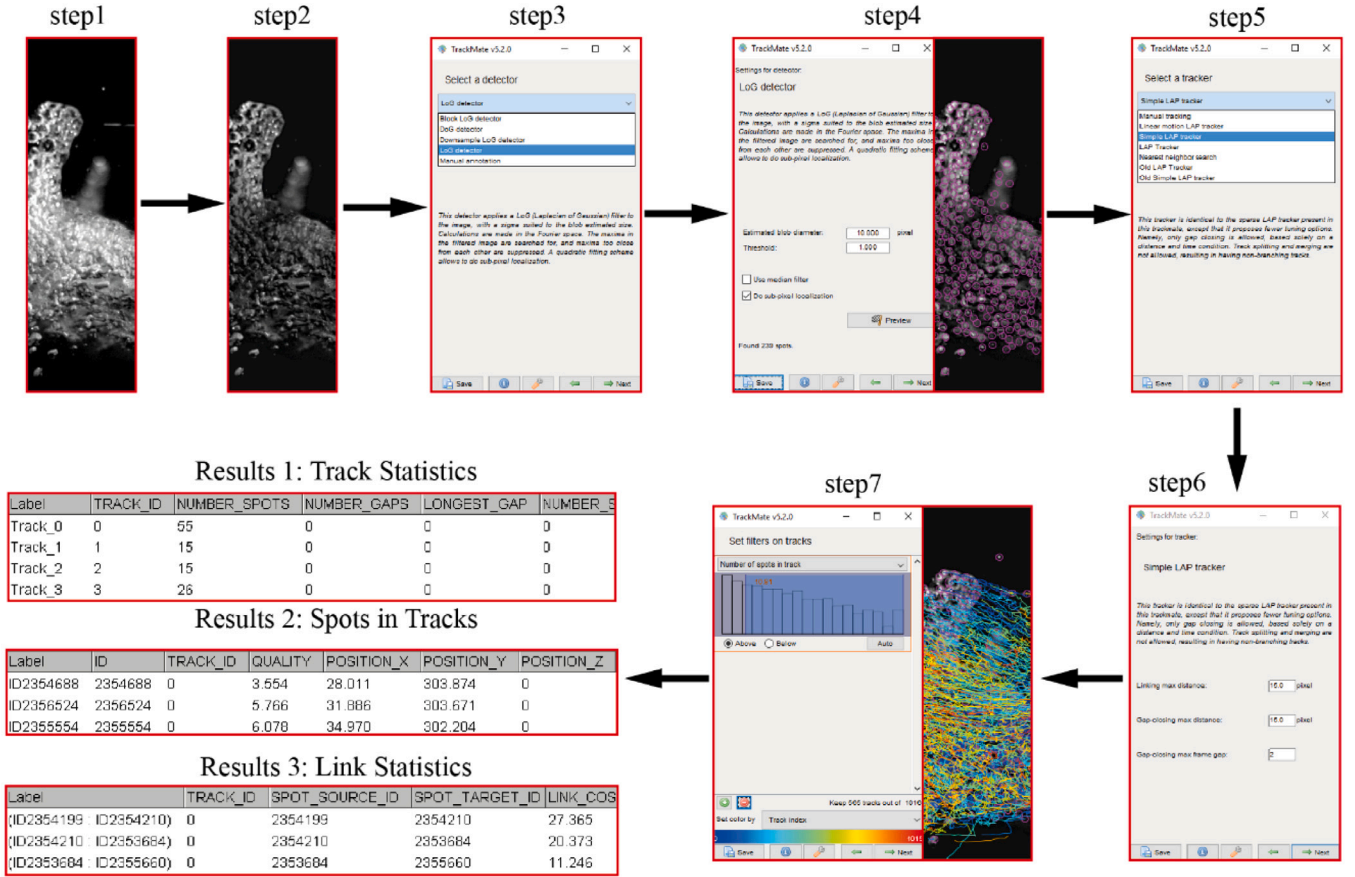
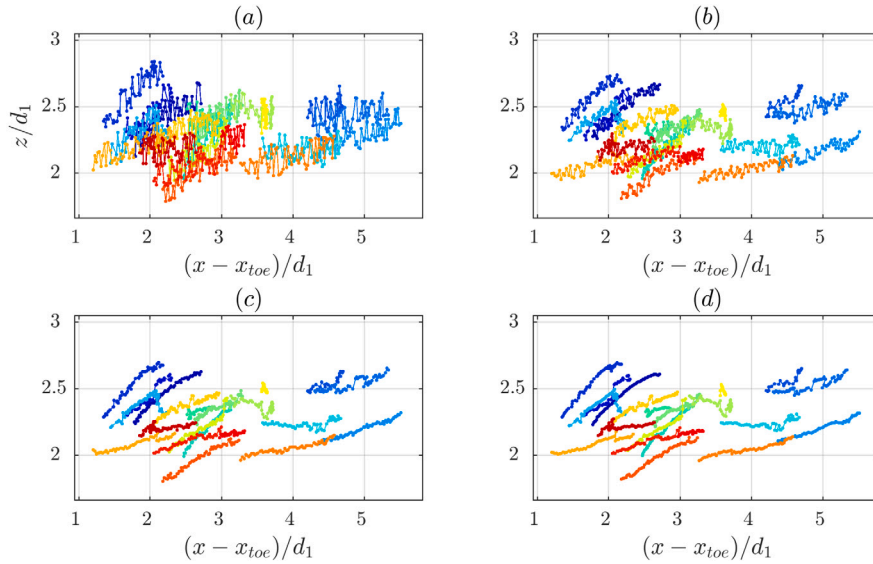**Fig. 8.** Applications of TrackMate on the immediate downstream of roller toe in breaking bore.

Fig. 9. Tracking trajectories of same particles for different subsampling frame rates (a) 5000 fps (b) 3000 fps (c) 1000 fps and (d) 1000 fps. The bore propagated from right to left.

data contained some negative values. A higher concentration of points shortly after the bore passage ($t < 1$ s) indicated the presence of more bubbles identified by the SBED technique, highly linked to some better correlation of the bubbly motion and higher void fraction near the roller toe. For all locations, the flow decelerated after the bore arrival, corresponding to a decay in velocity magnitude with increasing time. This was consistent with the velocity profiles underneath fully breaking

bores (Leng and Chanson, 2016). Similar distributions were observed between the centreline and sidewall data.

The data-retention rate P_R was defined as the ratio of the data satisfying the filtering criteria (Appendix A) to the total number of air chords, as shown in the right column of Fig. 11. A large amount of data was rejected, with similar distributions observed for both centreline and sidewall data. A higher data-retention rate occurred
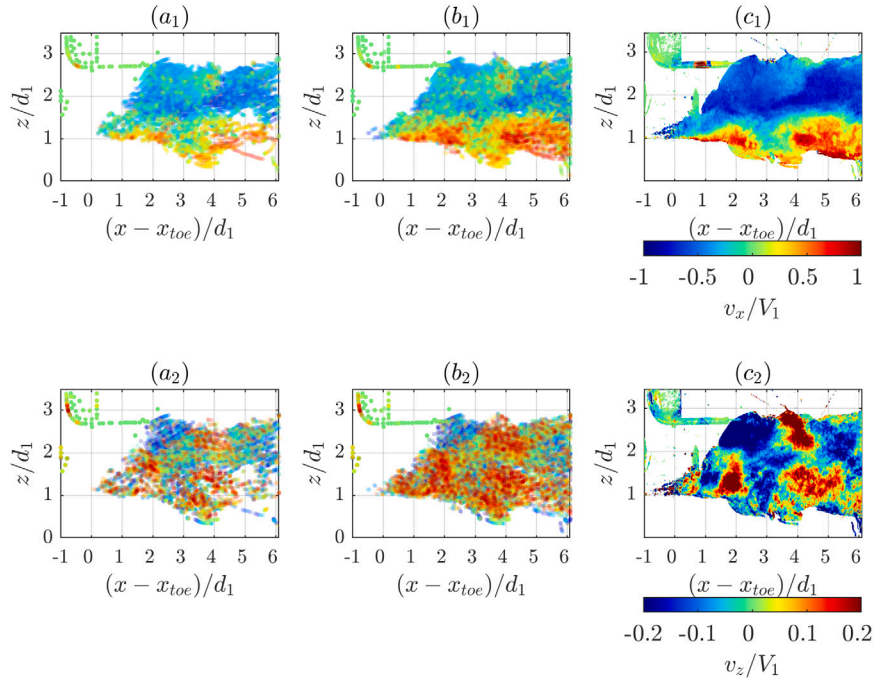
Fig. 10. Ensemble distributions of the instantaneous velocity fields using OF and PTV techniques. Top and bottom rows indicated the longitudinal and vertical velocity respectively: (a) PTV data for $D_L = 10$ pixels, $D_G = 10$ pixels, $F_G = 2$ frames and $T_{thres} = 15$ frames (b) $D_L = 10$ pixels, $D_G = 10$ pixels, $F_G = 2$ frames and $T_{thres} = 20$ frames; (c) optical flow data. Note the bore propagated from right to left.
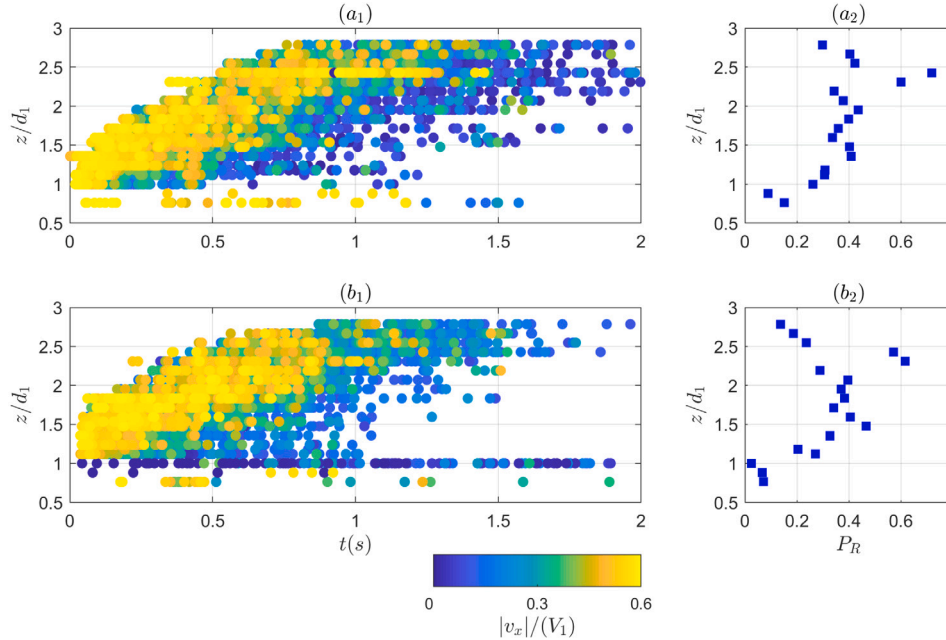

Fig. 11. Pseudo-instantaneous velocity ensemble distributions obtained with SBED technique at 20 vertical locations with 100 repetitions for each tests: (a_1) centreline velocity (a_2) data-retention rate on centreline (b_1) sidewall velocity (b_2) data-retention rate next to the sidewall. Note the bore propagated from right to left.

in the flow reversal region, where the longitudinal bubble advection was less impacted by the large-scale coherent structures than this in the developing shear layer. In the developing shear layer and free-surface regions, the presence of the large-scale coherent structures enhanced the bubble-turbulence interplay, corresponding to the lowest data-retention rate.

The OF velocity data were calculated in the Eulerian frame of reference. Following the synchronisation technique by Shi et al. (2021), the ensemble-averaged longitudinal ($V_{x,EA}$) and vertical ($V_{z,EA}$) velocities were obtained from 50,000 instantaneous OF values, as shown in

Fig. 12, where x_{toe} is the longitudinal coordinate of the roller toe. The longitudinal velocity data showed that the impinging flow decelerated from the roller toe, and that the velocity in the large recirculation zone compared well with the mean bore celerity. The vertical velocities were smaller than the longitudinal velocities in terms of magnitude. For $(x - x_{toe})/d_1 > 4$, the vertical velocity data were mainly positive, suggesting that the bubbly flow was driven by buoyancy. A marked shear layer was observed above the impinging flow, and limited data were obtained below the impinging flow in absence of bubbles.
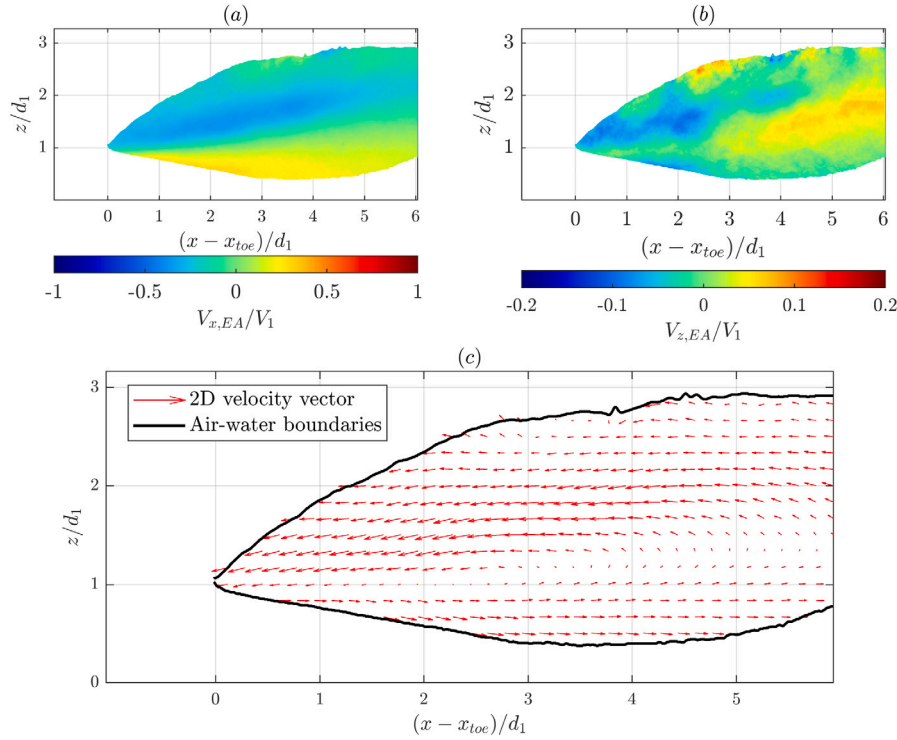
Fig. 12. Ensemble-averaged optical flow velocity fields: (a) longitudinal velocity field (b) vertical velocity field (c) two-dimensional vector field. The air–water boundaries were plotted and the bore propagated from right to left.

5.2. Lagrangian velocity data using PTV technique

The PTV technique was applied to the same 50,000 frames used for the OF approach, providing the trajectories of air–water flow patterns. The instantaneous velocity data were further derived from these trajectories, and were mapped into a structured grid using a data restructuring method modified from Aleixo et al. (2011). The data restructuring method consisted in (1) dividing the image plane in a $m \times n$ grid, (2) relocating the instantaneous velocity data into the grid based on the relative location from the roller toe (Shi et al., 2021) and (3) averaging instantaneous velocity data in each grid bin. Care must be taken for the selection of grid size. Large grid size would over-filter the velocity data, while a small grid size had inadequate data in some local regions. In the present study, the grid size was insensitive to the final velocity contour map, because of the enormous dataset, and a 8×8 pixel grid was selected as an optimum between accuracy and processing time. Fig. 13 presents the grid-averaged contour maps of longitudinal $V_{x,p}$ and vertical $V_{z,p}$ velocity. Cut-off boundaries are defined as the main body of air–water regions in the breaking bore, removing the droplet ejections above the free surface and occasional bubbly motions beneath the shear layer. The cut-off boundaries were obtained from manual tracking, shown as the black line in Fig. 13. The grid-averaged velocity contours agreed well with ensemble-averaged OF velocity contours (Fig. 12), in terms of the trends and magnitude.

Several vertical profiles of OF and PTV velocity data at different longitudinal locations are shown in Fig. 14, where the first and second rows are the longitudinal and vertical velocity data. The OF data were down-sampled by the 8×8 pixel grid, consistent with the size of grid-averaged PTV velocity fields. The comparison showed a better agreement downstream of the roller, e.g. $(x - x_{toe})/d_1 \geqslant 2.5$. The PTV technique provided more scattered velocity profiles than OF technique, which might be caused by uneven number of data used for the grid-averaging across the image plane.

6. Discussion

6.1. A comparison between proposed techniques

It was difficult to conduct a direct comparison on the results using these three techniques. The comparisons between the SBED, OF and PTV dataset showed good agreements, but also pointed out some differences. Herein, the measure of differences between the three techniques might be characterised by the probability density functions (PDFs) of their instantaneous velocity data, as shown in Fig. 15. Note that the SBED technique only provided the longitudinal velocity, and that the extreme velocity data, defined as $|v_x$ or $v_z/V_1| > 0.5$, regrouped on the both ends of PDFs. The comparisons of PDFs highlighted a global consistency. All PDFs of v_x exhibited a bimodal distribution, while the PDFs of v_z were similar to a normal distribution. Since three techniques were based on different principles, some differences could be expected. Furthermore, the different size of datasets for the three techniques would enhance the differences in PDFs.

Quantitatively, the angular difference approach was introduced to measure the deviation between averaged velocity data of OF and PTV techniques. The present angular difference was defined as (Baker et al., 2011), :

$$\psi_E = \cos^{-1}\left(\frac{1 + \overline{V_x}V_{x,EA} + \overline{V_z}V_{z,EA}}{\sqrt{1 + \overline{V_x}^2 + \overline{V_z}^2}\sqrt{1 + V_{x,EA}^2 + V_{z,EA}^2}} \right) \quad (9)$$

The angular difference was used to benchmark the performance of optical flow algorithms, providing the bias in degree (°) between the calculated and true velocity vectors. Herein, the ensemble-averaged velocity fields (Fig. 12) were down-sampled by the 8×8 grid, consistent with the grid-averaged PTV results (Fig. 13). Fig. 16 presents the distribution of angular error between the two averaged velocity contours. Large differences were observed in the shear layer of the breaking bore roller, where the rapidly evolving turbulence structures led to complex motion and extremely small turbulent length and time
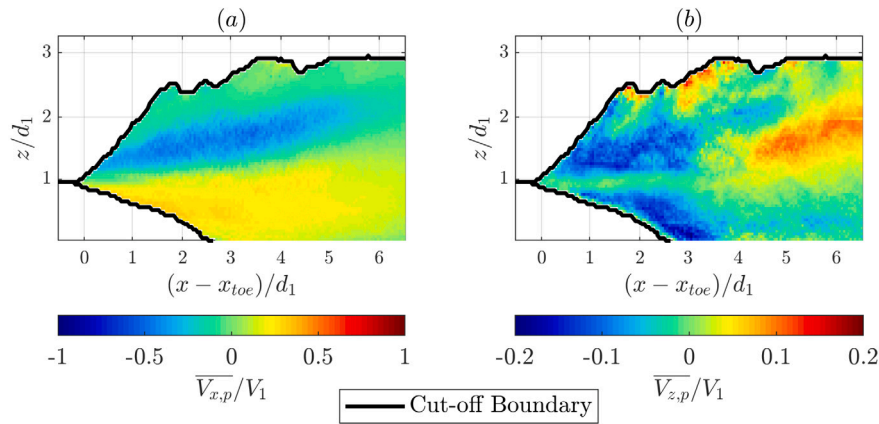
Fig. 13. Grid-averaged velocity contour maps based upon PTV (a) longitudinal velocity (b) vertical velocity. The bore propagated from right to left.
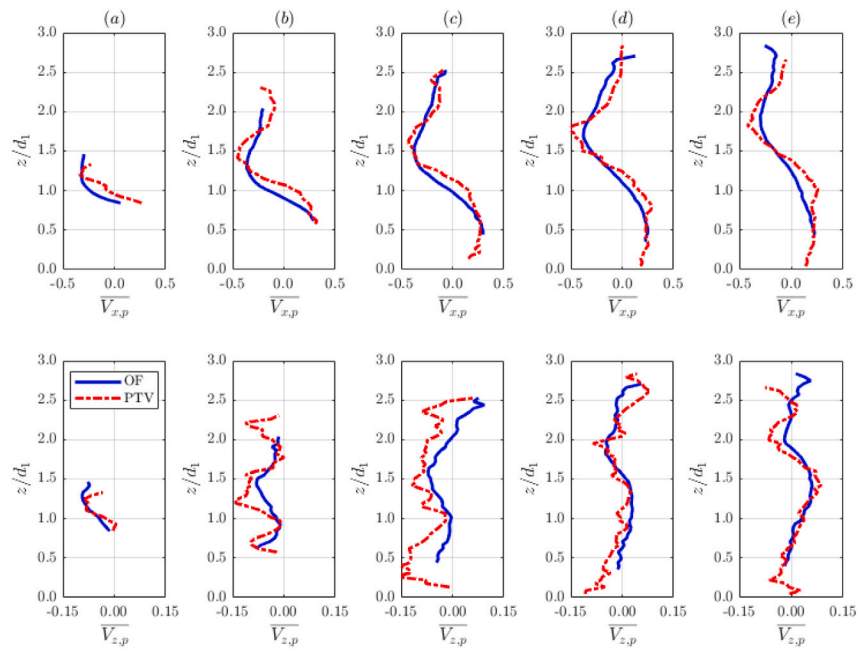

Fig. 14. Comparison of vertical profiles between OF and PTV longitudinal (first row) and vertical (second row) data (a) $(x - x_{toe})/d_1 = 0.5$, (b) 1.5, (c) 2.5, (d) 3.5, (e) 4.5.
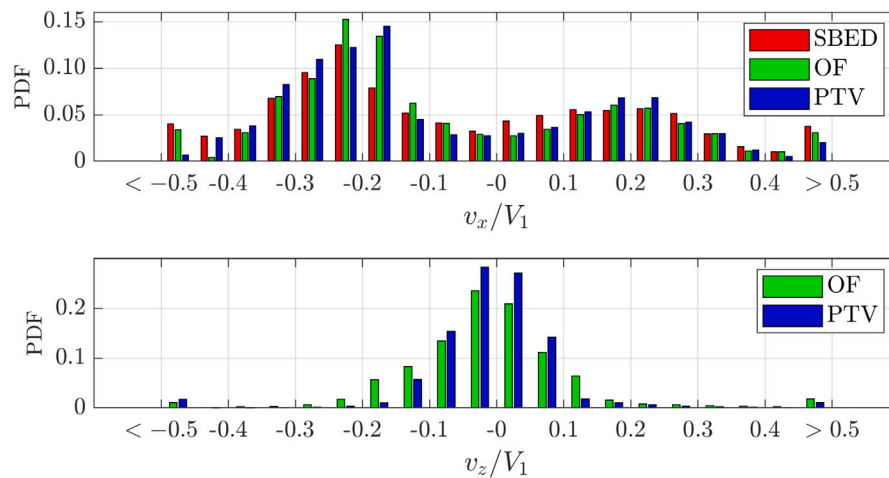

Fig. 15. Probability density function of instantaneous velocity data using SBED, OF and PTV techniques (a) longitudinal velocity (b) vertical velocity.
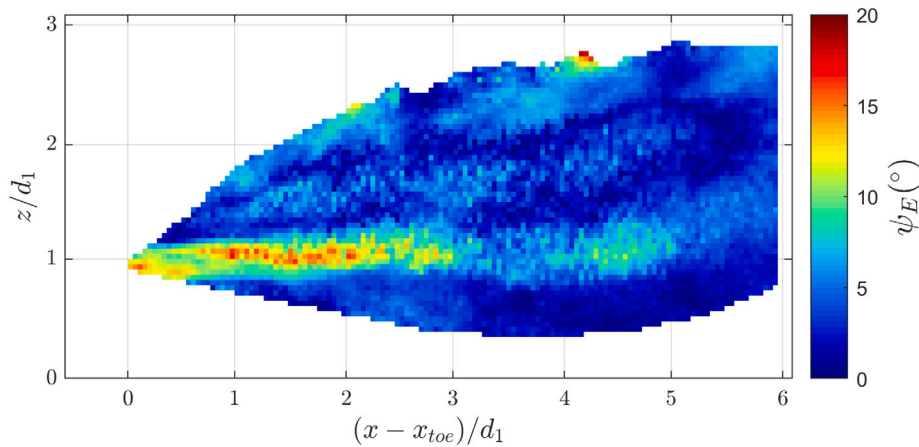
Fig. 16. The distribution of angular error between ensemble-averaged OF velocity and grid-averaged PTV velocity.

scales, challenging the pattern recognition with both OF and PTV techniques. To address the differences, further investigations would be required to implement localised models for the shear layer region, and advancing the existing OF and PTV algorithms.

6.2. Best robust velocity measurements in unsteady gas–liquid flow

Overall, since the real velocity value remains unknown, one cannot definitely state which technique provided more accurate velocity measurements than the others. In this subsection, the limitations of the proposed techniques are clearly highlighted, and a best practice of velocity measurements in unsteady gas–liquid flow is suggested.

Accurate velocity data obtained from experiments require high-quality raw signal and suitable signal processing techniques. In gas–liquid flows, the meaningful signals can be obtained by taking advantages of the differences between gas and liquid (phase-detection probe), and directly visualising flow motion (image-based instrumentation). The complexity of signal processing techniques is proportional to the void fraction and turbulence level. The higher void fraction and turbulence level indicate more active bubble dynamics, such as bubble breakup, collision and coalescence. Thus, additional filtering methods need to be applied to the signal processing of gas–liquid flows. For example, the main peak of the cross-correlation function could be higher than the threshold of the maximum cross-correlation coefficient R_{thres}, but providing a velocity magnitude over 10 times of the bore celerity, because of the extremely short window of the single bubble event. This was likely caused by a bubble splitting into several bubbles that were adjacent each others under the same coherent structures. Therefore, additional filters, namely the threshold of the ratio between interfacial travel621time and window duration W_{thres} and second peak ratio of the cross-correlation function SPR_n, were introduced to minimise the noise of bubble dynamics. For the image-based techniques, special care needs to be considered for the image noise. In the present PTV technique, several filtering parameters were used to deal with the noise from the camera, high void fraction and bubble dynamics. The multi-filtering criteria inevitably rejected a large amount of data, which might include some high-quality ones. Thus, it is crucial to have a validation dataset obtained with different approaches, making sure the data not over-filtered. On the other hand, the transient nature of unsteady gas–liquid flow provided limited data using pointwise measurements, including the low number of bubbles detected using phase-detection probe. For the experiments requiring long preparation periods (e.g. dam-break wave), a meaningful dataset require a large amount of resources.

The high void fraction, strong turbulence and unsteadiness generated many uncertainties for the velocity quantification in unsteady gas–liquid flows. The present three techniques of intrusive and non-intrusive velocimetry performed well in the highly aerated region,

although the filtering criteria can significantly impact on the results. For the most robust velocity measurements in unsteady gas–liquid flows, it is suggested to apply all three techniques, and the validation must be achieved by obtaining consistent results between the three techniques.

6.3. Limitations

Some the major challenges of the SBED technique are acknowledged herein, hopefully. At this stage, the turbulence estimation using the probe array was not achieved. For the AWCC technique applied in steady flow, the turbulence intensity was estimated in the small windows, where the velocity could be time-averaged (Kramer et al., 2020). This approach was considered meaningless in the breaking bore, where the velocity dropped rapidly during the bore passage. Secondly, the bore impacting the intrusive probe tip generated more turbulence in the flow. Hence, the measurements in the breaking bore tended to be more difficult to get meaningful longitudinal data, compared to the steady flows (i.e. stationary hydraulic jump). This led to a large amount of data rejected from the filtering process. Lastly, although many bubbles were observed in the breaking bore, not many were detected from the probe tip. 100 runs for each locations were considered time consuming but necessary at the same time.

For the image-based techniques (OF and PTV), the measurements were limited to the sidewall region. The high void fraction blocked any visualisation from the channel centreline. This was a common challenge in any experimental studies in highly aerated gas–liquid flows using image-based approach, which has not been resolved from the literature. The parameters adopted in the image-based techniques required a validation study for different flow scenarios, because of the different bubble-turbulence interactions. A universal set of parameter seems to be impossible in this case.

Overall, above limitations are the well-known challenges in air–water flow studies. Addressing above limitations is considered as a long-term research goal, and idea of this paper is to advance the experimental quantification of air–water properties into the regime of unsteady flow by introducing novel intrusive and non-intrusive approaches.

7. Conclusion

The present study presented the development and application of intrusive and non-intrusive techniques of velocimetry in the unsteady gas–liquid flows with high void fraction. The breaking bore, as a classic unsteady air–water flow, was selected for the application of these techniques. Both intrusive phase-detection probes and high-speed videos were used to get the air–water flow signals in the breaking bore.
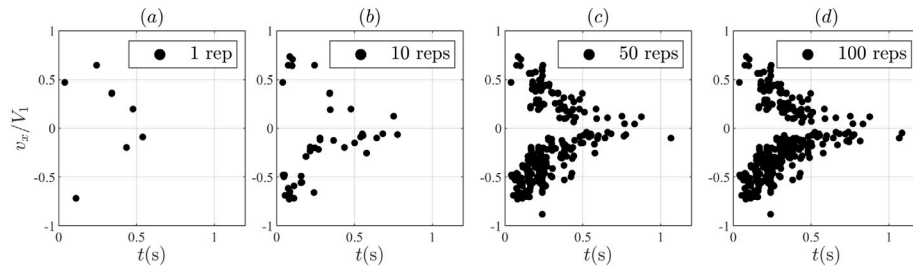
Fig. A.1. Sensitivity analysis in terms of number of repetitions to obtain the ensemble-pseudo-instantaneous velocity at $(z - d_1)/d_1 = 0.36$ for centre probe. Filtering criteria: $W_{thres} = 0.3$, $R_{thres} = 0.4$ and $SPR_{thres} = 0.5$.
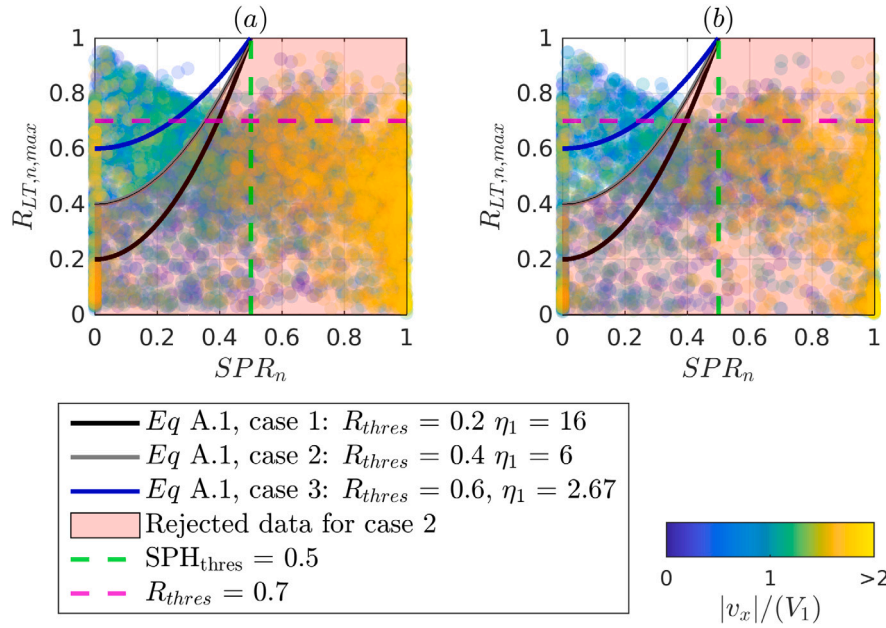

Fig. A.2. A dimensionless relationship between ensemble-pseudo-instantaneous velocity magnitude $|v_x|/V_1$, $R_{LT,n,max}$ and secondary peak ratio SPR_n, with $W_{thres} = 0.3$ (a) centreline data (b) sidewall data.

In the Eulerian frame of references, the single bubble event detection (SBED) technique was derived using phase-detection probes based on the concept of individual bubble event. The SBED technique computes the pseudo-instantaneous interfacial velocity for individual bubble events. Three filtering criteria were applied to improve the data quality, and their impacts on the velocity estimation were quantitatively examined. In the breaking bore, limited velocity data were obtained due to the restrictive filtering criteria and few bubble events detected per test, leading to ensemble-instantaneous velocity from 100 repetitions. The velocity data of SBED technique were comparable with the image-based velocity data using an optical flow (OF) technique. A comprehensive velocity dataset, containing 20 locations, was collected. For the velocity trends, the velocity magnitude data exhibited a rapid decay after the bore passage, and a good agreement was seen between centreline and sidewall data. For the Lagrangian approach, particle tracking velocimetry (PTV) was applied using the open source package ImageJ. The PTV was able to highlight the trajectories of air–water flow features, which was used to obtain grid-averaged velocity contours.

For further quantitative comparisons between the results from the SBED, OF and PTV techniques, the differences were characterised by the probability distributions of their instantaneous velocity data. The PDF of longitudinal velocity showed a bimodal distribution, with positive and negative peaks corresponding to the predominate velocity in the shear layer and the recirculation region respectively. The limitations of the proposed techniques were further discussed. For the three techniques, the multi-filtering criteria were essential to minimise

the impacts of bubble dynamics, turbulence and unsteadiness on the data quality. Nevertheless, it is important to mention that none of these techniques should be solely applied to obtain robust interfacial velocity in unsteady gas–liquid flows. For best velocity measurements in unsteady gas–liquid flow, it is suggested that the high-quality data require all three techniques to give consistent velocities.

CRediT authorship contribution statement

Rui Shi: Conceptualization, Methodology, Software, Formal analysis, Visualization, Writing – original draft. **Davide Wüthrich:** Conceptualization, Methodology, Software, Formal analysis, Visualization, Writing – original draft, Project administration. **Hubert Chanson:** Conceptualization, Methodology, Writing – review & editing, Supervision.

Declaration of competing interest

The authors declare the following financial interests/personal relationships which may be considered as potential competing interests:In line with recommendations of the Office of the Commonwealth Om-620budsman (Australia) and International Committee on Publication Ethics621(COPE), Hubert Chanson has a conflict of interest with Matthias Kramer622(UNSW Canberra).

Data availability

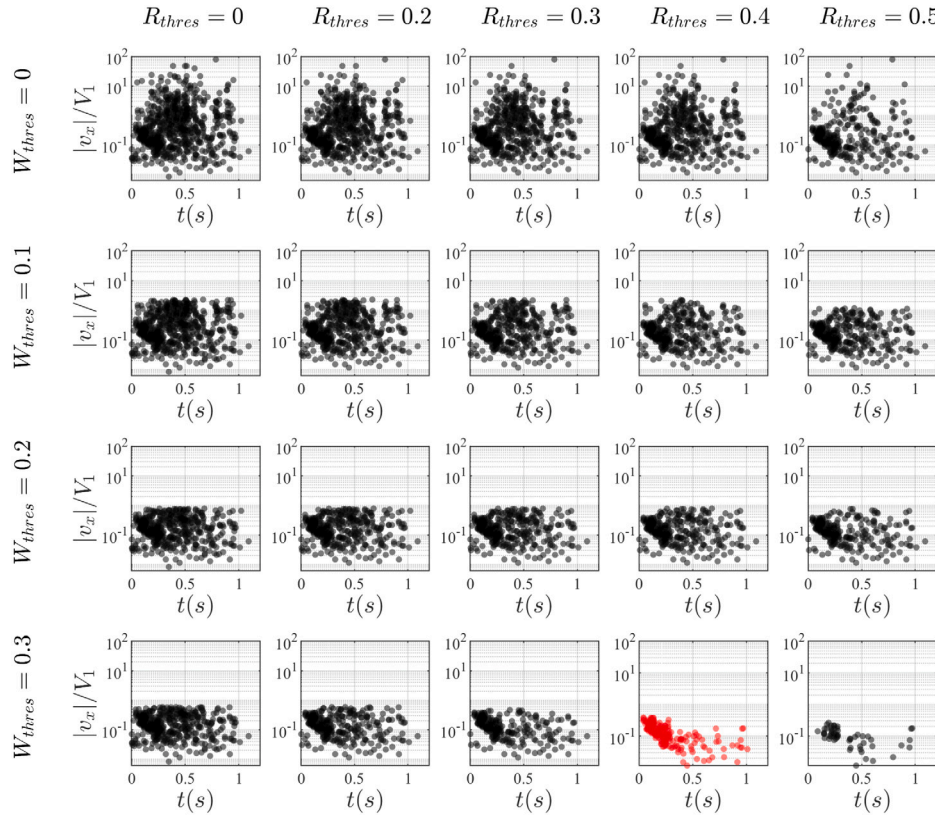Data will be made available on request.

Fig. A.3. Sensitivity analysis of W_{thres} and R_{thres} with $SPR_{thres} = 0.5$. The most suitable filters provided the data in red. (For interpretation of the references to colour in this figure legend, the reader is referred to the web version of this article.)

Acknowledgements

Appendix A. Sensitivity analyses in SBED technique

A.1. Number of repetitions

Multiple repetitions were required to obtain a trend of ensemble-pseudo-instantaneous velocity, a single test usually detected limited bubbles, in which a part of single bubble event was rejected from the filtering criteria (Appendix A.2). Herein, a sensitivity analysis was performed to obtain the minimum number of repetitions. Fig. A.1 shows the ensemble-pseudo-instantaneous velocity profile for 1, 10, 50 and 100 repetitions. Overall, the negative data were consistent with the bore propagation direction. 1 and 10 repetitions were not enough to provide a trend, while 50 repetitions provided enough data points to obtain the decreasing velocity magnitude with increasing time. 100 repetitions provided a dense dataset, particularly for $t > 0.6$ s. Overall, the sensitivity analysis indicated that a minimum of 50 repetitions was

required to obtain a reliable ensemble-pseudo-instantaneous velocity dataset using SBED technique in highly unsteady free-surface flow. The present study adopted 100 repetitions for the velocity estimations.

A.2. Filtering techniques

Several filters were applied to improve the data quality. The performance of the SBED technique depends on the selection of a number of filtering criteria: including the threshold of the maximum cross-correlation coefficient R_{thres}, the threshold of secondary peak ratio of the cross-correlation function SPR_{thres}, and the threshold of the ratio between interfacial travel time and window duration W_{thres}. The velocity data were retained when $R_{LT,n,max} > R_{thres}$, $|T_n|/W_n > W_{thres}$ and $SPR_n < SPR_{thres}$. For the R_{thres} value, Herringe and Davis (1976) and Hu et al. (1998) adopted $0.2 \leq R_{thres} \leq 0.5$ for PIV data, while Matos et al. (2002) and Kramer et al. (2019) used $R_{thres} = 0.7$ and $R_{thres} = 0.5$ respectively for the velocity measurements using phase-detection probes in steady air–water flow. The threshold SPR_{thres} was introduced to minimise the impact of bubbly dynamics on the velocity measurements. Keane and Adrian (1990) suggested a high value range of SPR_{thres} (0.7–0.8), compared to $SPR_{thres} = 0.6$ used by Kramer et al. (2019) in steady flows. The W_{thres} was a novel filtering threshold, responsible for removing extreme values.

The SPR_{thres} and R_{thres} were selected first with a constant W_{thres} value, since Kramer and Chanson (2019) suggested a negative correlation relationship between SPR_n and $R_{LT,n,max}$. An empirical equation was used to determine the optimum of SPR_n and $R_{LT,n,max}$ values based on the velocity data:

$$\frac{R_{LT,n,max}}{\eta_1 SPR_n^2 + 1} > R_{thres} \tag{A.1}$$

where η_1 is coefficient calculated from selected R_{thres}. Fig. A.2 presents the pseudo-instantaneous velocity magnitude with the filtering criteria

of Eq. (A.1), for $W_{thres} = 0.3$ on the centreline and next to the sidewall. A outlier was defined as $|v_x|/V_1 > 2$, and $SPH_n = 0.5$ was considered to filter the most of outliers. Three cases of Eq. (A.1) shows that too much data were rejected for $R_{thres} = 0.6$, and that $R_{thres} = 0.2$ was considered too small from the literature. Therefore, the middle value of $R_{thres} = 0.4$ was used.

The impacts of SPR_{thres} and W_{thres} on the velocity data were further investigated, and the sensitivity analysis is presented in Fig. A.3. Overall, the results showed that the combination of both filters significantly reduced the number of velocity outliners. The application of W_{thres} removed the data, which had a low cross-correlation coefficient and a small time lag relative to the time window. The small time lag might suggest the different bubble events in the leading and trailing tip signals, because of the bubble dynamics and bubble transverse movement in the highly turbulent bore roller. Practically, the velocity tended to decrease with increasing time after the bore passage at a given location (Leng and Chanson, 2016). This was consistent with the case of $R_{thres} = 0.4$ and $W_{thres} = 0.3$, marked as the red dot in Fig. A.3.

Appendix B. Optical flow

The Gunnar–Färnback (GF) OF technique (Farnebäck, 2003) was proved to provide accurate air–water interfacial velocity from the sidewall in both steady (Bung and Valero, 2016; Zhang and Chanson, 2018) and unsteady flow (Shi et al., 2020). The GF technique assumes that the brightness intensity data before and after the displacement followed a quadratic function as:

$$f_1(X_{im}) = X_{im}^T A_{f1} X_{im} + b_{f1}^T X_{im} + c_{f1} \tag{B.1}$$

where X_{im} is the coordinate vector in the image plane A_{f1} and b_{f1} are the coefficient matrices, c_{f1} is a constant matrix. The subscript 1 means the first image, and superscript T means the matrix transposition. A displacement d_f takes place in the following image, following:

$$\begin{aligned} f_1(X_{im} + d_f) &= (X_{im} - df)^T A_{f1}(X_{im} - d_f) + b_{f1}^T(X_{im} - d_f) + c_{f1} \\ &= (X_{im}^T A_{f2} X_{im}) + b_{f2}^T X_{im} + c_{f2} \end{aligned} \tag{B.2}$$

The Eqs. (B.1) and (B.2) the same constant coefficient matrices for the quadratic function, yielding:

$$d_f = \frac{1}{2}(bf_1 - bf_2) \tag{B.3}$$

The above equation was numerically solved in a small neighbourhood of pixels, instead of a pointwise estimation, because of noise problem. By summing the local constraints in the neighbourhood, the OF functional became a minimisation problem.

The GF technique was implemented in the Computer Vision Toolbox in MATLAB2019a. Several parameters impacted on the results, including the neighbourhood size N_{OF}, filtering size F_{OF}, pyramid level L_{OF}. The neighbourhood size and filtering size were used to minimise the noise during and after computation respectively. The Toolbox included the image pyramid to address large displacement between the two images. The previous studies suggested a reliable velocity estimation using GF technique with $N_{OF} = 5$, $F_{OF} = 15$ and $L_{OF} = 2$ (Shi et al., 2020), which were used in the present study. The ultra-high-speed videos were subsampled to 5000 fps for the OF computation (Zhang and Chanson, 2018).

References

Abràmoff, M.D., Magalhães, P.J., Ram, S.J., 2004. Image processing with ImageJ. Biophotonics Int. 11 (7), 36–42.

Ahmadi, F., Ebrahimian, M., Sanders, R.S., Ghaemi, S., 2019. Particle image and tracking velocimetry of solid-liquid turbulence in a horizontal channel flow. Int. J. Multiph. Flow. 112, 83–99.

Aleixo, R., Soares-Frazão, S., Zech, Y., 2011. Velocity-field measurements in a dam-break flow using a PTV Voronoï imaging technique. Exp. Fluids 50 (6), 1633–1649.

Bachalo, W., 1994. Experimental methods in multiphase flows. Int. J. Multiph. Flow. 20, 261–295.

Baker, S., Scharstein, D., Lewis, J., Roth, S., Black, M.J., Szeliski, R., 2011. A database and evaluation methodology for optical flow. Int. J. Comput. Vis. 92 (1), 1–31.

Brocchini, M., Peregrine, D., 2001. The dynamics of strong turbulence at free surfaces. Part 1. description. J. Fluid Mech. 449, 225–254.

Bung, D.B., Valero, D., 2015. Image processing for bubble image velocimetry in self-aerated flows. In: 36th IAHR World Congress. pp. 6594–6601.

Bung, D.B., Valero, D., 2016. Optical flow estimation in aerated flows. J. Hydraul. Res. 54 (5), 575–580.

Cartellier, A., 1992. Simultaneous void fraction measurement, bubble velocity, and size estimate using a single optical probe in gas–liquid two-phase flows. Rev. Sci. Instrum. 63 (11), 5442–5453.

Cartellier, A., Achard, J., 1991. Local phase detection probes in fluid/fluid two-phase flows. Rev. Sci. Instrum. 62 (2), 279–303.

Chang, K.-A., Lim, H.-J., Su, C.B., 2003. Fiber optic reflectometer for velocity and fraction ratio measurements in multiphase flows. Rev. Sci. Instrum. 74 (7), 3559–3565.

Chanson, H., 2005. Air–water and momentum exchanges in unsteady surging waters: an experimental study. Exp. Therm Fluid Sci. 30 (1), 37–47.

Chanson, H., 2012. Tidal Bores, Aegir, Eagre, Mascaret, Pororoca: Theory and Observations. World Scientific.

Chanson, H., Toombes, L., 2002. Air–water flows down stepped chutes: turbulence and flow structure observations. Int. J. Multiph. Flow. 28 (11), 1737–1761.

Crowe, C., Schwarzkopf, J., Sommerfeld, M., Tsuji, Y., 1998. Multiphase Flows with Droplets and Particles. CRC Press.

Cummings, P.D., 1996. Aeration due to breaking waves (Ph.D. thesis). The University of Queensland.

Farnebäck, G., 2003. Two-frame motion estimation based on polynomial expansion. In: Scandinavian Conference on Image Analysis. Springer, pp. 363–370.

Fuchs, T., Hain, R., Kähler, C.J., 2017. Non-iterative double-frame 2D/3D particle tracking velocimetry. Exp. Fluids 58 (9), 1–5.

Hanus, R., 2015. Application of the Hilbert transform to measurements of liquid–gas flow using gamma ray densitometry. Int. J. Multiph. Flow. 72, 210–217.

Herringe, R.t., Davis, M., 1976. Structural development of gas-liquid mixture flows. J. Fluid Mech. 73 (1), 97–123.

Hu, H., Saga, T., Kobayashi, T., Okamoto, K., Taniguchi, N., 1998. Evaluation of the cross correlation method by using PIV standard images. J. Vis. 1 (1), 87–94.

Jaqaman, K., Loerke, D., Mettlen, M., Kuwata, H., Grinstein, S., Schmid, S.L., Danuser, G., 2008. Robust single-particle tracking in live-cell time-lapse sequences. Nature Methods 5 (8), 695–702.

Jones Jr., O.C., Delhaye, J.-M., 1976. Transient and statistical measurement techniques for two-phase flows: a critical review. Int. J. Multiph. Flow. 3 (2), 89–116.

Keane, R.D., Adrian, R.J., 1990. Optimization of particle image velocimeters. I. Double pulsed systems. Meas. Sci. Technol. 1 (11), 1202.

Kiger, K.T., Duncan, J.H., 2012. Air-entrainment mechanisms in plunging jets and breaking waves. Annu. Rev. Fluid Mech. 44, 563–596.

Kimmoun, O., Branger, H., 2007. A particle image velocimetry investigation on laboratory surf-zone breaking waves over a sloping beach. J. Fluid Mech. 588, 353–397.

Kocamustafaogullari, G., Wang, Z., 1991. An experimental study on local interfacial parameters in a horizontal bubbly two-phase flow. Int. J. Multiph. Flow. 17 (5), 553–572.

Kramer, M., Chanson, H., 2019. Optical flow estimations in aerated spillway flows: Filtering and discussion on sampling parameters. Exp. Therm Fluid Sci. 103, 318–328.

Kramer, M., Hohermuth, B., Valero, D., Felder, S., 2020. Best practices for velocity estimations in highly aerated flows with dual-tip phase-detection probes. Int. J. Multiph. Flow. 126, 103228.

Kramer, M., Valero, D., Chanson, H., Bung, D.B., 2019. Towards reliable turbulence estimations with phase-detection probes: an adaptive window cross-correlation technique. Exp. Fluids 60 (1), 1–6.

Leng, X., Chanson, H., 2016. Coupling between free-surface fluctuations, velocity fluctuations and turbulent Reynolds stresses during the upstream propagation of positive surges, bores and compression waves. Environ. Fluid Mech. 16 (4), 695–719.

Leng, X., Chanson, H., 2019. Two-phase flow measurements of an unsteady breaking bore. Exp. Fluids 60 (3), 1–15.

Lighthill, J., 1978. Waves in Fluids. Cambridge University Press.

Liu, T., Bankoff, S., 1993. Structure of air-water bubbly flow in a vertical pipe—II. Void fraction, bubble velocity and bubble size distribution. Int. J. Heat Mass Transfer 36 (4), 1061–1072.

Lubin, P., Kimmoun, O., Véron, F., Glockner, S., 2019. Discussion on instabilities in breaking waves: Vortices, air-entrainment and droplet generation. Eur. J. Mech. B Fluids 73, 144–156.

Matos, J., Frizell, K.H., André, S., Frizell, K.W., 2002. On the performance of velocity measurement techniques in air-water flows. In: Hydraulic Measurements and Experimental Methods 2002. pp. 1–11.

Na, B., Chang, K.-A., Lim, H.-J., 2020. Flow kinematics and air entrainment under laboratory spilling breaking waves. J. Fluid Mech. 882.

Neal, L., Bankoff, S., 1963. A high resolution resistivity probe for determination of local void properties in gas-liquid flow. AIChE J. 9 (4), 490–494.

Nezu, I., Sanjou, M., 2011. PIV and PTV measurements in hydro-sciences with focus on turbulent open-channel flows. J. Hydro-Environ. Res. 5 (4), 215–230.

Oliveira, J., Van der Geld, C., Kuerten, J.G., 2015. Lagrangian velocity and acceleration statistics of fluid and inertial particles measured in pipe flow with 3D particle tracking velocimetry. Int. J. Multiph. Flow. 73, 97–107.

Peregrine, D.H., 1983. Breaking waves on beaches. Annu. Rev. Fluid Mech. 15 (1), 149–178.

Ryu, Y., Chang, K.-A., Lim, H.-J., 2005. Use of bubble image velocimetry for measurement of plunging wave impinging on structure and associated greenwater. Meas. Sci. Technol. 16 (10), 1945.

Ryu, Y., Chang, K.-A., Mercier, R., 2007. Runup and green water velocities due to breaking wave impinging and overtopping. Exp. Fluids 43 (4), 555–567.

Sene, K., 1984. Aspects of bubbly two phase flow (Ph.D. thesis). University of Cambridge.

Serizawa, A., Kataoka, I., Michiyoshi, I., 1975. Turbulence structure of air-water bubbly flow—I. Measuring techniques. Int. J. Multiph. Flow. 2 (3), 221–233.

Shi, R., Leng, X., Chanson, H., 2020. On optical flow techniques applied to breaking surges. Flow Meas. Instrum. 72, 101710.

Shi, R., Leng, X., Chanson, H., 2021. Breaking bore roller characteristics: Turbulence statistics using optical techniques. Coast. Eng. 168, 103893.

Stansby, P., Chegini, A., Barnes, T., 1998. The initial stages of dam-break flow. J. Fluid Mech. 374, 407–424.

Tinevez, J.-Y., Perry, N., Schindelin, J., Hoopes, G.M., Reynolds, G.D., Laplantine, E., Bednarek, S.Y., Shorte, S.L., Eliceiri, K.W., 2017. TrackMate: An open and extensible platform for single-particle tracking. Methods 115, 80–90.

Wang, H., Chanson, H., 2019. Characterisation of transverse turbulent motion in quasi-two-dimensional aerated flow: application of four-point air-water flow measurements in hydraulic jump. Exp. Therm Fluid Sci. 100, 222–232.

Warsito, W., Fan, L.-S., 2001. Measurement of real-time flow structures in gas–liquid and gas–liquid–solid flow systems using electrical capacitance tomography (ECT). Chem. Eng. Sci. 56 (21–22), 6455–6462.

Wüthrich, D., Shi, R., Chanson, H., 2021. Strong free-surface turbulence in breaking bores: a physical study on the free-surface dynamics and air–water interfacial features. J. Fluid Mech. 924.

Zhang, G., Chanson, H., 2018. Application of local optical flow methods to high-velocity free-surface flows: Validation and application to stepped chutes. Exp. Therm Fluid Sci. 90, 186–199.

Ziegenhein, T., Lucas, D., 2019. The critical bubble diameter of the lift force in technical and environmental, buoyancy-driven bubbly flows. Int. J. Multiph. Flow. 116, 26–38.